Chapter 8
Discovering High-Pressure and High-Temperature Minerals

Oliver Tschauner and Chi Ma

Abstract Defining high-pressure (P) and high-temperature (T) minerals beyond vague conventions requires robust criteria. The conjunction of mineralogy and (mantle-)geochemistry suggests that pressure-dependent ionic radii provide such a criterion. A set of quantitative arguments is provided based on the pressure-dependent radii of several elements. Three categories and regimes of high-P minerals are defined. All approved high-pressure minerals are tabulated here. High-pressure minerals form under static and dynamic pressure. Under dynamic compression the short duration of the peak pressure state acts as a kinetic barrier for transformations. Only local high temperature ('hotspots') permits formation of high-pressure minerals. Very high temperature of extreme shock compression induces retrograde conversion of high-pressure minerals or melting during the passing of the rarefaction wave. Only few metastable high-pressure silicate minerals (and even synthetic phases) have been observed in shocked rocks and samples: Even along temperature gradients we find metastable formation of phases stable at lower static pressures but few minerals without stability field, despite the multitude of possible metastable structures. This suggests sterical hindrance of the Si[4] → [6] transition, besides the kinetic barrier. In the deep Earth high-pressure minerals in the deep Earth are hidden from direct observation. Hypothesized retrograde transformations in peridotites and of inclusions in diamonds remain to be confirmed. Few occurrences of high-pressure minerals as inclusions in diamonds have been reported. In conjunction with their hosting mineral, diamond, they appear to have formed in regions of mantle metasomatosis, and potentially mark regions or horizons of extensive chemical mobility within the mantle. Consistent with the definition of high-P minerals we define a high P–T regime and we propose to define high-T minerals that form at low or ambient pressure through the T-induced changes in redox buffer systems. This approach encompasses the rich mineralogy of presolar and early solar minerals which cover a compositional range

O. Tschauner (✉)
Department of Geoscience, University of Nevada Las Vegas, 4505 Maryland Parkway, Las Vegas 89154, USA
e-mail: oliver.tschauner@unlv.edu

C. Ma
Division of Geological and Planetary Sciences, Caltech, MC 170-25, Pasadena, CA 91125, USA

L. Bindi and G. Cruciani (eds.), *Celebrating the International Year of Mineralogy*,
Springer Mineralogy, https://doi.org/10.1007/978-3-031-28805-0_8

far beyond the occurrences in differentiated planetary bodies like Earth, Mars, and Moon.

Keywords Minerals · Pressure · Earth mantle · Shock · Ionic radii · Early condensates · Meteorites

8.1 The Concept and the Chemistry of High Pressure Minerals

The distinction of high-pressure and high-temperature minerals from minerals that form under less extreme conditions requires criteria that define pressures and temperatures as either high or low. It is useful to examine the effect of the two parameters, pressure and temperature, initially as separate. We find that the range of energy that is compatible with the crystalline state of matter that involves changes only in pressure exceeds by far the range of changes induced only by temperature, with regard to the crystalline state: The materials with the highest melting points melt between 2000 and 3000 K at ambient pressure (Adachi and Imanaka 1998). These temperatures correspond to energies in the range of ¼−1/3 eV/at, if we simply multiply the temperatures with the Boltzmann constant. However, the change in energy that occurs upon compressing mantle peridotite from the shallow lithosphere to the core mantle boundary over an interval of about 136 GPa of pressures is in the range of 1.6 eV/at: With an approximate bulk composition of Mg_2SiO_4, ¾ of the Earth's mantle are oxygen as constituent chemical species and within this approximation the compression of the O^{2-} anion dominates the increase of the electronic contribution to the inner energy of bulk silicate Earth over the entire range of compression by amount and size (Tschauner 2022a). Between 0 and 136 GPa (the pressure of the core mantle boundary) the contraction of the crystal radius of O^{2-} is from about 1.26 to $1.16{\cdot}10^{-10}$ m (Tschauner 2022a) (Fig. 8.1a), hence: $4/3\pi{\cdot}\Delta r^3 \cdot 1.36{\cdot}10^{11}$ N/m^2 = $2.50{\cdot}10^{-19}$ J/at = 1.56 eV/at (of O^{2-}). Yet, throughout this range of pressure mantle rock remains in the solid state along the average geotherm. Thus, within the range of the solid state, pressure as a parameter allows for changes in energy several times larger than temperature, even within the limited range of conditions that occur inside Earth. Since the melting points of solids generally increase with pressure, a regime of high temperatures that corresponds to energy changes of $\geq$ 1 eV/at and that is compatible with the solid state occurs only at sufficiently high pressures.

High-pressure and high-temperature minerals involve constituent chemical species whose valence electron configuration is energeticaly favourable at the pressures and temperatures of formation of these minerals but are unfavourable or unstable at low pressures and ambient conditions (Tschauner 2019). Radial valence electron distributions, that is: ionic radii and crystal radii, are sufficient to define these criteria. Ionic and crystal radii represent spherical spatial averages over a multitude of different bond states (Rahm et al. 2020; Tschauner 2022a, b). Although the radii neglect the actual bond states of the individual compounds and structures, they allow

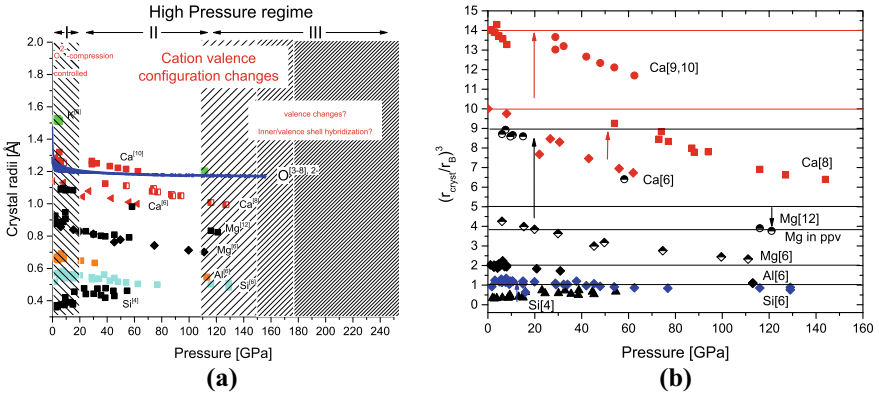

Fig. 8.1 Crystal radii of geochemically abundant elements as functions of pressure. **a**: Radii of K,Mg,Ca, Al, Si and O^{2-} in different bond coordination by O^{2-}. Radii of O are corrected for coordination by the cations. **b**: Ionic volumes normalized by the Bohr radius r_B. Reconstructive transitions to high-pressure minerals and phases are indicated by arrows. Data are from Tschauner (2022a) with additions based on data by Dewaele et al. (2012), Levien et al. (1980), Lazarz et al. (2019), Ko et al. (2022), Richet et al. (1988). The pressure dependencies are r(K[8]) = 1.62(2)–0.003(1)P; r(Ca[6]) = 1.143(3)–0.00239(8)P; r(Ca[7,8]) = 1.188(7)–0.00149(8)P; r(Ca[9,10]) = 1.319(8)–0.0020(2)P; r(Mg[6]) = 0.856(7)–0.0015(1)P; r(Mg[12]) = 1.11(3)–0.0024(1); r(Al[6]) = 0.669(2)–0.00108(4)P; r(Si[4]) = 0.373(9) + 0.0020(3)P; r(Si[6]) = 0.567(3)–0.00095(9)P. P in GPa and radii in Å

for assessing types of structure that are assumed by solids of very different composition or stability fields. This point is well illustrated by the successful application of tolerance factors and similar criteria that correlate composition with crystal structure types (e.g. in Li et al. 2004) and their evolution with pressure (e.g. Manjon et al. 2007).

Pressure shifts compounds into structure types which are generally assumed by compounds of chemical species with higher nuclear charge number at ambient pressure (Shannon and Prewitt 1969). For instance, bridgmanite, the high-pressure polymorph of $MgSiO_3$ is isotypic with perovskite, $CaTiO_3$, davemaoite, the high-pressure polymorph of $CaSiO_3$, is isotypic with tausonite, $SrTiO_3$, stishovite SiO_2 is isotypic with rutile, TiO_2, the high-pressure minerals lingunite, liebermannite, stöfflerite assume the structure of hollandite $KMn^{3+}Mn^{4+}{}_3O_8$ and so on (see Table 8.1). This general trend has been interpreted as result of the stronger compression of the anions relative to the cations (Downs and Prewitt 1998), but it also indicates relative changes of cation ionic radii with pressure (see Fig. 8.1). A quantitative concept of these pressure effects allows for correlating mantle geochemistry with high-pressure mineralogy and petrology. The effect of pressure on the crystal radii is shown in Fig. 8.1a for K^+, Mg^{2+}, Ca^{2+}, Al^{3+}, Si^{4+}, and O^{2-} in different bond coordination (henceforth, formal valences are not specified and bond coordination is given in angular brackets). The following observations are made: (a) The O-anion exhibits initially a marked non-linear compression converging towards weaker linear compression. (b) All cations exhibit linear contraction over the examined pressure intervals (Fig. 8.1a) within uncertainties. Only Si[4] expands with pressure. (c)

Heavier cations like K and Ca are more compressible than lighter ones like Mg, Al, and Si. d) The higher the charge the lesser the pressure effect, see Fig. 8.1, caption). (e) A general trend for the pressure dependence of crystal radii with bond coordination is not seen for the available data. In part these basic pressure-induced trends have been noticed previously (Shannon and Prewitt 1969; Downs and Prewitt 1998; Gibbs et al. 2012) but actual compressibilities were only recently reported for some bonded radii (Gibbs et al. 2012), some crystal radii (Tschauner 2022a), for non-bonding radii (Rahm et al. 2020) and, by means of corresponding states, for Wigner–Seitz radii of elemental metals (Tschauner 2022b). In the caption of Fig. 8.1 we give the compressibilities for Mg,Al,Si,K,Ca which are based on an augmented set of data and where the change of the O-anion radius with anion coordination (Shannon 1976) is taken into account in calculating the cation crystal radii. It is noteworthy that the fitted crystal radii at 1 bar match Shannon's radii very well although 1 bar radii were not used as fix points (see caption Fig. 8.1). The only fitted 1 bar radius that deviates from Shannon's radii is that of Si[6].

Figure 8.1a shows that with increasing pressure a regime controlled by strong nonlinear O^{2-} contraction is followed by a regime of reduced, nearly linear contraction. In this regime contraction of larger cations K and Ca is more prominent than that of O (Fig. 8.1a). The border between the two regimes coincides with the Si[4] → [6] transition and, thus, delineates the boundary between low- and intermediate-pressure silicates (Tschauner 2019) on one side, and high-pressure silicates on the other side (Table 8.1). Here we define these two regimes as 'high-pressure I' and 'high pressure II' (Fig. 8.1). The radii of Ca[8] and [10] in CaO-B1 and in davemaoite interpolate to the 1 bar crystal radii of Ca[7] and [9], respectively (Fig. 8.1 caption). If one accepts the notion that radii represent spherical spatial averages of valence electron configurations (Rahm et al. 2020; Tschauner 2022a,b), this coordination change suggests a gradual change of the valence electron configuration for Ca over about ½ Mbar of linear compression.

The compression of radii by 10–30% (Fig. 8.1a) is well within the range of differences between radii of different chemical species or different valences of the same species. In Fig. 8.1b ionic volumes r_{cryst}^3 are normalized by the cube of the Bohr radius r_B. The volumes of Si, Al, Mg, and Ca in six-fold coordination by O^{2-} are approximately one-,two, four- and ten-times r_B^3 (lines in Fig. 8.1b). Sixfold Mg, Al, and Ca approach Si[6] between 170–180 GPa by extrapolation of their linear pressure-depencencies, Ca[8-10] between 290–300 GPa. At those pressures, the contraction of the O anion is small, thus, volume reducing transitions either have to involve a change in cation coordination and valence electron structure or a change in valence of O (Zhu et al. 2013). Significant volume reduction may involve hybridization of inner shell electrons with the valence electron states. This tentative 'ultra-high pressure regime' is labeled as 'high-pressure III' in Fig. 8.1a. The bridgmanite-ppv transition (Murakami et al. 2004; Ono and Oganov 2004) may indicate the onset of this regime (although without hybridization of inner and valence shell electrons). Consequently, we classify high-pressure minerals based these three regimes as hPI, hPII, hpIII. However, the process is generally not as straightforward: reconstructive pressure-induced phase transitions appear to reset the electron density. In CaO the

Table 8.1 List of all approvedminerals from the high-pressure regimes hP-II and -III. Some petrologically related incipient high-pressure minerals (Tschauner 2019) from regime hP-I are listed also (printed in italics). Endmember composition, first reference of the approved mineral or announcement by the CNMNC, density of endmembers and the density of the stable polymorph at reference conditions are given. The reported densities of the type specimens of these minerals may be different if they contain noticeable amounts of other components. In Occurrences, references are given only if different from the type material reference. (natural high-pressure phases that are not approved minerals)

Name	Composi-tion	Structure type	Reference of type	Density g/cm^3	Occurrence
Elements and alloys					
Diamond	C	Diamond	–	3.516 (graphite: 2.26)	Kimberlites, lamproites, impactites, meteorites (shock-induced transformation and presolar)
Lonsdaleite	C	Diamond-2H	Chao (1967)	3.5–3.6 (graphite: 2.26)	The type material has been shown to be defect-rich diamond (Nemeth et al. 2014), but the mineral is not discredited
Deltanitrogen	N_2	™*loc-*N_2	Navon et al. (2017), Tschauner et al. (2022a, b)	™*loc-*$N_2$1.767 (–)	Inclusions in diamonds exsolution from N-bearing diamonds from Junia, Brazil
Hexaferrum	Fe	Mg	Mochalov et al. (1998)	8.26 (iron: 7.88)	(Earth's core, potentially as accessory in the lower mantle), in serpentinites and in CAI's stabilized by PGEs (Ma 2012)

(continued)

Table 8.1 (continued)

Name	Composi-tion	Structure type	Reference of type	Density g/cm^3	Occurrence
Icosahedrite	$Al_{63}Fe_{24}Cu_{13}$	Quasicrystal	Bindi et al. (2011)		In the Khatyrka carbonaceous chondrite, formation in shock-generated metallic melt (Asimow et al. 2016), see Chap. 1
Pnictides and Chalcogenides					
Allabogdanite	Fe_2P	β-Fe_2P	Britvin et al. (2002)	6.86 (barringerite: 5.90)	In shocked iron-meteorites. Metastable in pyrometamorphic rocks of the Hatrurim-formation (Galuskin et al. 2022)
Q uingsongite	BN	Sphalerite	Dobrzhinetzkaya et al. (2014)	3.488 (h-BN: 2.298)	Luobushao, Tibet
Shenzhuangite	$NiFeS_2$	Chalcopyrite	Bindi et al. (2018)		In the highly shocked Suizhou L6 meteorite
Zolenskyite	$FeCr_2S_4$	Ordered NiAs	Ma and Rubin (2022)	4.09 (daubréelite: 3.83)	In the Indarch EH4 enstatite chondrite, likely from debris of highly shocked material that was entrapped in the Indarch partent body

(continued)

Table 8.1 (continued)

Name	Composi-tion	Structure type	Reference of type	Density g/cm^3	Occurrence
Molecular Minerals					
Ice-VII	H_2O	Anti-cuprite with macroscopic disorder of H on site 8a	Tschauner et al. (2018a)	2.07 (ice-Ih: 0.95)	As inclusions in diamonds and probably in the interior of icy moons and planets
(Ice-VI)	H_2O	Ice-VI	Kagi et al. (2000)		Not an approved mineral, detected by IR-spectroscopy as inclusion in a diamond. Probably in the interior of icy moons
(CO_2-I)	CO_2	Related to Pyrite	Schauder and Navon (1993)	1.76[1] (−)	As inclusions in diamond and in comets
Oxides and Hydroxides					
Coesite	SiO_2	Coesite (a feldspar like arrangement of tetrahedral network	Chao et al. (1960)	3.04 (quartz: 2.65)	In impact-metamorphic quartz-bearing rocks, in meteorites, in eclogites, and as inclusion in diamonds

(continued)

Table 8.1 (continued)

Name	Composi-tion	Structure type	Reference of type	Density g/cm^3	Occurrence
Stishovite	SiO_2	Rutile	Chao et al. (1962)	4.28 (quartz: 2.65)	In impact-metamorphic quartz-bearing rocks, n lunar and in chondritic meteorites
Seifertite	SiO_2	Scrutinyite	Dera et al. (2002), El Goresy et al. (2008)	4.3 (quartz: 2.65)	In the Shergotty martian meteorite
Srilankite	TiO_2	Scrutinyite	Willgallis et al. (1983)	4.39 (rutile: 4.25)	In granulite-facies, in metasomatized mantle (Wang et al. 1999), and in impact-metamorphic rocks, from rutile (formerly described as 'TiO_2-II'(El. Goresy et al. 2001a, b)
Riesite	TiO_2	Riesite	Tschauner et al. (2020a)	4.37 (rutile: 4.25)	In impact-metamorphic rocks, retrograde from akaogiite
Akaogiite	TiO_2	Baddeleyite	ElGoresy et al. (2001a, b)	4.72 (rutile: 4.25)	In impact-metamorphic rocks, after rutile,
Scrutinyite	PbO_2	Scrutinyite	Taggart et al. (1988)	9.87 (plattnerite: 9.70)	In oxidation zones of ore deposits together with plattnerite, in hydrothermal veins

(continued)

Table 8.1 (continued)

Name	Composi-tion	Structure type	Reference of type	Density g/cm^3	Occurrence
Lingunite	$NaAlSi_3O_8$	Hollandite	Gillet et al. (2000)	3.6 (albite: 2.6)	In shock-transformed albitic clasts and at the border of shock melt-veins and-pockets in meteorites and in impact-metamorphic rocks (Agarwal et al. 2016)
Liebermannite	$KAlSi_3O_8$	Hollandite	Ma et al. (2018)	3.9 (orthoclase: 2.7)	In shock-transformed orthoclase-rich clasts and at the border of shock melt-veins and -pockets in meteorites and in impact-metamorphic rocks (Stähle et al. 2022)
Stöfflerite	$CaAl_2Si_2O_8$	Hollandite	Tschauner et al. (2021a)	4.0 (anorthite:2.7)	In shock-transformed plagioclase clasts and at the border of shock melt-veins and-pockets in meteorites and in impact-metamorphic rocks

(continued)

Table 8.1 (continued)

Name	Composi-tion	Structure type	Reference of type	Density g/cm^3	Occurrence
Wadsleyite	Mg_2SiO_4	Wadsleyite, a spinelloid	Price et al. (1983)	3.6 (forsterite: 3.2)	Shock-transformed forsterite within and at the border of shock melt-veins in meteorites (Tomioka and Miyahara 2017), (in Earth's transition zone, not directly observed)
Asimowite	Fe_2SiO_4	Wadsleyite	Bindi et al. (2019)	4.8 (fayalite: 4.4)	Shock-transformed fayalite in the Suizhou L6 and the Quebrada Chimborazo 001 CB3.0 chondrites. Component of terrestrial wadsleyite (not directly observed)
Ringwoodite	Mg_2SiO_4	Spinel	Binns et al. (1969)	3.8 (forsterite: 3.2)	Shock-transformed forsterite within and at the border of shock melt-veins and–pockets in meteorites, in a diamond from the Earth's transition zone (Gu et al. 2022)

(continued)

Table 8.1 (continued)

Name	Composi-tion	Structure type	Reference of type	Density g/cm^3	Occurrence
Ahrensite	Fe_2SiO_4	Spinel	Ma et al. (2016)	4.85 (fayalite: 4.4)	Shock-transformed fayalite at rim of shockmelt pockets in the Tissint SNG meteorite, (component of ringwoodite in the transition zone)
Ringwoodite-Q	$(Mg,Fe,Si)_2(Si,\square)O_4$	Spinel	Ma et al. (2019d)	3.59	At the rim of shock melt pockets in the Tenham and Suizhou L6 chondrites
Ahrensite-Q	$(Fe,Mg,Cr,Ti,Ca,\square)_2(Si,Al)O_4$	Spinel	Ma et al. (2019b)	3.95	At the rim of shock melt pockets in the Tissint shergottite
Poirierite	Mg_2SiO_4	Spinelloid	Tomioka et al. (2021)	3.326 (forsterite: 3.2)	In the highly shocked Tenham and Suizhou L6 chondrites, probably retrograde during rapid decompression at relatively low temperature
Elgoresyite	$Mg_5Si_2O_9$	$Ca_3Tl_4O_9$	Bindi et al. (2021)	4.315	In a shock-induced melt vein of the Suizhou L6 chondrite

(continued)

Table 8.1 (continued)

Name	Composi-tion	Structure type	Reference of type	Density g/cm^3	Occurrence
Maohokite	$MgFe_2O_4$	$CaTi_2O_4$-type	Chen et al. (2017)	5.33 (magnesio-ferrite: 4.5)	In the Suizhou LG chondrite, from shock transformation. A possible component of postspinel oxides in subducted lithospheric slabs (not directly observed)
Chenmingite	$FeCr_2O_4$	$CaFe_2O_4$-type	Ma et al. (2019c)	5.6 (chromite: 5.1)	Shock-Transformed chromite in meteorites
Xieite	$FeCr_2O_4$	$CaTi_2O_4$-type	Chen et al. (2003)	5.8 (chromite: 5.1)	Shock-transformed chromite in meteorites. Possibly in subducted lithospheric slabs (not directly observed)
Tschaunerite	$FeTi_2O_4$	$CaTi_2O_4$-type	Ma et al. (2021a)	5.5 (ulvøspinel: 5.0)	Shock-transformed ulvøspinel in meteorites. Possibly in subducted lithospheric slabs (not directly observed)

(continued)

Table 8.1 (continued)

Name	Composi-tion	Structure type	Reference of type	Density g/cm^3	Occurrence
Feiite	$(Fe,Ti)_4O_5$	Galenobismuthite	Ma et al. (2021c)	5.4 (wüstite + ulvøspinel: 5.6)	Reaction zone of shocked ulvøspinel with shock-induced melt in the Shergotty meteorite. Possibly in subducted lithospheric slabs (not directly observed, Woodland et al. 2013)
Akimotoite	$MgSiO_3$	Ilmenite	Tomioka and Fuji-no (1997, 1999). Tschauner et al. (2018b)	3.8 (enstatite:3.2)	Shock-transformed enstatite clasts within shock-melt veins of chondrites. Within the shock-melt matrix of Acfer040 (Sharp et al. 1997)
Hemleyite	$FeSiO_3$	Ilmenite	Bindi et al. (2017)	4.8[3] (ferrosilite:3.6)	In shock-transformed ferrosilite from the Suizhou L6 chondrite
Wangdaodeite	$FeTiO_3$	$LiNbO_3$	Xie et al. (2016); Tschauner et al. (2020b)	4.9 (ilmenite: 4.8)	Retrograde from luite in shock-transformed clasts in melt veins from terrestrial impactites

(continued)

Table 8.1 (continued)

Name	Composi-tion	Structure type	Reference of type	Density g/cm^3	Occurrence
Liuite	$FeTiO_3$	Perovskite	Ma et al. (2021c)	5.5 (ilmenite: 4.8)	Shock Transformed ilmenite in SNC meteorites. Possibly in subducted lithospheric slabs (not directly observed)
Zagamiite	$CaAl_2Si_{3.5}O_{11}$	'CAS'	Ma et al. (2017b), (2019a), Beck et al. (2004)	3.4–3.6	In Ca-Al-rich shock-melt pockets in SNC meteorites. Possibly in deeply subducted Ca-Al rich rocks
Donwilhelmsite	$CaAl_1Si_{4.5}O_{11}$	'CAS'	Fritz et al. (2020)	3.4–3.6	In Ca-Al rich shock-melt pockets in a lunar meteorite. Possibly in deeply subducted Ca-Al rich rocks

(continued)

Table 8.1 (continued)

Name	Composi-tion	Structure type	Reference of type	Density g/cm^3	Occurrence
Davemaoite	$CaSiO_3$	Tausonite	Tschauner et al. (2021b), (2022d)		As inclusion in diamonds from the deep transition zone or lower mantle (Nestola et al. 2018; Tschauner et al. 2021b). Vitrified in highly shocked meteorites (Gosh et al. 2021)
Bridgmanite	$MgSiO_3$	Perovskite, $GdFeO_3$-type	Tschauner et al. (2014)	4.1 (enstatite:3.2)	In shock-transformed enstatite clasts in shock melt-veins of chondrites and at the rim of shock-melt pockets in the Tissint Shergottite (Ma et al. 2016). There are unconfirmed claims that enstatite inclusions in some diamonds are retrograde bridgmanite, e.g.: (Stachel et al. 2000)
Hiroseite	$Fe(Si,Fe)O_3$	Perovskite, $GdFeO_3$-type	Bindi et al. (2020)		Solid state transformation of ferrosilite in the Suizhou L6 chondrite

(continued)

Table 8.1 (continued)

Name	Composi-tion	Structure type	Reference of type	Density g/cm^3	Occurrence
Dmitryivanovite	$CaAl_2O_4$	Harmunite, monoclinic distorted	Ivanova et al. (2002)	3.63 (krotite: 2.94)	In a CAI from the CH chondrite Northwest Africa 470
Silicates					
Reidite	$ZrSiO_4$	Scheelite	Glass et al. (2002)	5.16 (zircon: 4.67)	In terrestrial impactites (Glass et al. 2002) and as lamellae in detrital shocked zircon (Cavoisie et al. 2015)

(continued)

Table 8.1 (continued)

Name	Composi-tion	Structure type	Reference of type	Density g/cm^3	Occurrence
Majorite	$Mg_3(Mg,Si)_2Si_3O_{12}$	Garnet	Smith and Mason (1970)	3.8 (enstatite: 3.2)	In shock melt veins in chondrites and in terrestrial impactites. From transformed amphiboles at the rim of shock melt veins in terrestrial impactites (Stähle et al. 2011; Ma et al. 2021a, b, c), as component in garnets that occur as inclusion in diamonds (Collerson et al. 2010), as inclusion in diamond (Huang et al. 2020)
Jeffbenite	$Mg_3Al_2Si_3O_{12}$	'TAPP'	Harris et al. (1997), Nestola et al. (2016)	3.55 (pyrope: 3.55)	As inclusion in diamonds, forming at 6–10 GPa (Armstrong et al. 2008)
Breyite	$Ca_3Si_3O_9$	Walstromite	Brenker et al. (2021)	3.52 (wollastonite: 2.9)	As inclusion in diamonds, forming at 3–9 GPa (Anzollini et al. 2016; Litasov et al. 2014; Fedoraeva et al. 2019)

(continued)

Table 8.1 (continued)

Name	Composi-tion	Structure type	Reference of type	Density g/cm^3	Occurrence
Jadeite	$NaAlSi_2O_6$	Jadeite		3.47	In high-grade metamorphic rocks and as component of omphacite in eclogites. In shock-melt vein matrices in chondrites and terrestrial impactites, as inclusion in diamonds (Angel et al. 1992)
Albitic CPx	$Na(Al,.)Si_2O_6$	'Ca-Eskola-Cpx'	Ma et al. (2022b)	3.5	In shock-melt vein matrices in Shergottites and in chondritic meteorites, in terrestrial impactites; as component in eclogitic cpx (omphacite)
Tissintite	$Ca(Al,.)Si_2O_6$	'Ca-Eskola-Cpx'	Ma et al. (2015)	3.4 (kushiroite: 3.4)	In shock-melt vein matrices in Shergottites and chondrites. In terrestrial impactites, as component in eclogitic cpx (omphacite, Mc Cormick 1986)

(continued)

Table 8.1 (continued)

Name	Composi-tion	Structure type	Reference of type	Density g/cm^3	Occurrence
Ten-Å phase (TAP)	$(Mg,Al,\ldots)_3Si_4O_{10}(OH,F)_2\ 2H_2O$	Mica	Huang et al. (2020)		As inclusion in a diamond (Huang et al. 2020). Potentially abundant in hydrated mantle rock in subductions zones
Phosphates					
Tuite	$Ca_3[PO_4]_2$	Tuite	Xie et al. (2003)	3.47	Shock-transformed apatite and dehydrated whitlockite, in chondritic and Martian Meteorites

transition from the NaCl- to the CsCl-type around 40–60 GPa (Richet et al. 1988) resets the normalized volume of Ca[8] to that of Ca[6] at ambient pressure and so does the coordination change of Ca upon formation of davemaoite (Fig. 8.1b, red arrows). The transitions from Mg[6] to [12] and from Si[4] to [6] also increase the ionic volume (Fig. 8.1b, black and blue arrows). Hence, bulk volume contraction upon those transitions is result of the increased bond coordination of both, cation and anion, which generally allows for denser structural arrangements of the atoms (Downs and Prewitt 1998). The positive pressure-dependence of Si[4] and its volume smaller than r^3_B indicate indirectly the extensive overlap of Si–O binding orbitals. The reset of high-pressure crystal radii to larger radii upon high-pressure phase transitions is indicative of the changes in valence electron configuration, if we allow the radii to represent spherically symmetric spatial averages of these configurations (Rahm et al. 2020; Tschauner 2022a,b). This case becomes interesting, when high-pressure transitions induce radii that match those of other elements at low pressure: For instance, the crystal radius of Mg in $CaIrO_3$-type $MgSiO_3$ matches the crystal radius of Ca[6] extrapolated to the transition pressure of ~ 120 GPa (Fig. 8.1b). K[6] intersects Ca[9,10] between 32 and 40 GPa, Mg[12] intersects Ca[6] around 20 GPa and Ca[8] between 60 and 80 GPa. There is no known mineral where Ca[6] would substitute for Mg[6] around 20 GPa but the substitution Ca + Fe for Mg + Al in bridgmanite has been proposed to occur above 60 GPa in experimental work (Ko et al. 2022). Type davemaoite, $CaSiO_3$, contains a noticeable amount of K and Fe (Tschauner et al. 2021b, 2022a), consistent with a formation in the range of 20–30 GPa (Fig. 8.1a,b). Coordination changes reset the crystal ionic volumes (see above, Fig. 8.1b) but this effect is only indirectly expressed in solid solutions through changes in crystal chemical compatibility. In consequence, some but not all intersections of relative ionic volumes $(r_{cryst}/r_B)^3$ match the formation of high-pressure minerals or pressure-induced chemical substitution. The underlying chemical selection rules are beyond the topic of this chapter. Even at high pressure entropic components remain important and the phase diagrams do not simply reflect a sequence of pressure-induced transformations but include minerals and mineral assemblies that occur at combined elevated pressure and temperature (e.g. in Fig. 8.2). This is the case at least within the hPI and hPII regimes.

8.1.1 High Pressure Minerals–Their Occurrences

Minerals from the high-pressure regime I ('hpI') are found in high-grade metamorphic rocks such as eclogites and in xenoliths of garnet peridotites from below 60 km depth in the upper mantle. Several excellent reviews about these occurrences are available and it is not necessary to recapitulate this work here. Some of these intermediate pressure minerals are presented here along with the discussion of high-pressure minerals hPII and -III (Table 8.1). The occurrence of high-pressure minerals in Earth in the deep Earth is beyond direct access to us. However, four sources of these minerals have been found: meteorites, whose parent bodies have experienced

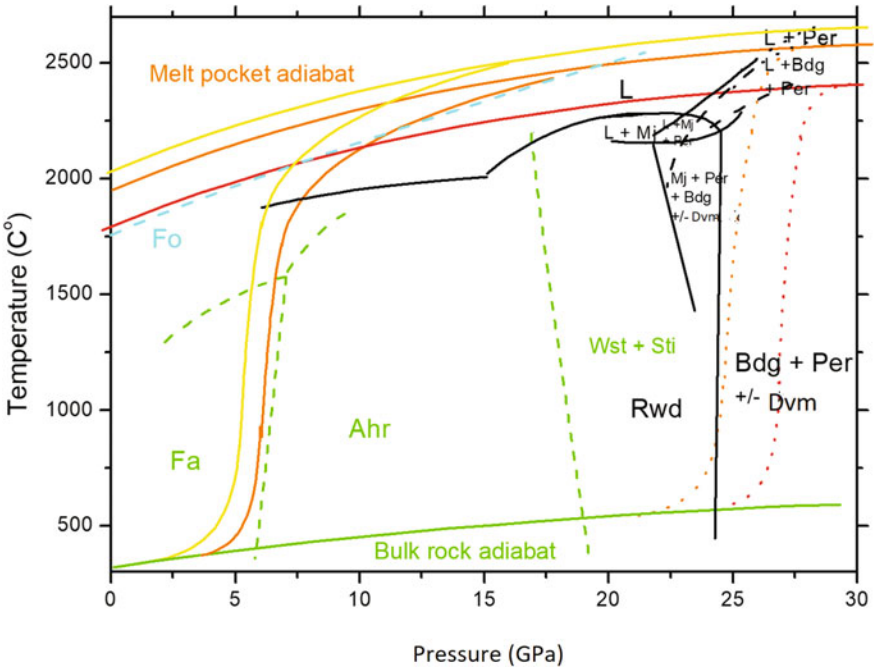

Fig. 8.2 Shock release path of melt pockets in the Tissint Shergottite. The pocket shown in Fig. 8.3a contains dense glass in the center and its main cooling occurred within the stability field of bridgmanite (red dotted lines). Another pocket contains intergrowth of pigeonite and fayalite in its center indicating cooling at much lower pressure (red and yellow lines). Thermodynamic phase boundaries are indicated for Fe_2SiO_4 (green, dashed) and the simplified CMS system (black), adiabats of the shock-generated melt (yellow and red lines) and the bulk rock (green) bracket the cooling paths. Data are taken from Ma et al. (2016)

strong shock-metamorphism by asteroid collisions, (b) terrestrial rocks that have experienced shock metamorphism through asteroid impacts, (c) inclusions in terrestrial diamonds. In addition (d) regimes of high pressures and temperatures occur in the ejecta of novae and supernovae part of whose debris is conserved as presolar grains in primitive meteorites, interplanetary and interstellar dust.

8.1.1.1 High-Pressure Minerals that Form Under Dynamic Compression

This section highlights some general aspects of high-pressure minerals that form under dynamic compression rather than the physics of shock and the processes that occur during shock-metamorphism.

Presolar dust grains are subject to extensive research mostly focusing on isotopic anomalies that witness nucleonic processes inside large stars and during supernovae.

These processes are beyond the stability of atomic matter and, therefore, beyond our topic. Nonetheless, the process of capturing matter in solid phases through sublimation in the cooling ejecta involves high temperatures (see Sect. 8.4) and may in part involve elevated pressures also. Because of the low density of the ejected gas the regime of high pressure at temperatures below the condensation point of solid phases is rather limited and may, for that reason, be restricted to diamond as the solid phase with the highest sublimation and melting point. Diamond is a common presolar mineral (Table 8.1). The occurrence of presolar diamonds with high density of stacking faults along [111] (Daulton et al. 1996) is consistent with formation at high dynamic stresses and stress-rates, (Armstrong et al. 2022). Periodic stacking faults along [111] lead to the formation of lonsdaleite, the 2H-polytype of diamond (Table 8.1). Metastable formation at low pressures provides an alternative explanation of presolar diamond, for instance, nano-diamond forms during combustion of acetylene. So far, no presolar high-pressure mineral other than diamond has been found.

Collision of small planetary bodies, so called 'planetesimals' were a process intrinsic to the early history of the solar system and have nurtured the formation the larger planets. Chondrules, that is: spherical aggregates of one or several minerals that are frequently found in many common meteorites ('s.c chondrites', Rubin and Ma 2017), have been suggested to be the quench products of shock-induced melting and spallation of these melt particles, but there are alternative explanations of chondrule formation (see Rubin and Ma 2017 for detailed discussion). Within the asteroid belt collisions continue to occur. For instance, one of the most common type of meteorites, L-chondrites, is debris from the disruption of a planetesimal during a collision that occurred in the asteroid belt in the Ordovicium (Greenwood et al. 2007). Principally, all meteorites that we find on Earth have experienced modifications through dynamic compression during the events that destroyed their parent body in large events or ejected them from their surface in smaller events. The range of petrographically documented shock-metamorphic processes ranges from a few GPa to > 70 GPa (Stöffler et al. 2018). These changes have been categorized based on shock-induced deformation features that have been observed both in experiments and in nature on a scale that ranges from S1 (0–5 GPa) to S6 (>70 GPa) (Stöffler et al. 2018). High-pressure minerals are observed in meteorites of the shock metamorphic categories S4 and above. States of dynamic compression during asteroid collisions are generally assessed to less than 1 s. In fact, most estimates suggest durations of 10–100 ms (Tschauner et al. 2009; Hu and Sharp 2017; Ma et al. 2016; Tomioka and Miyahara 2017), corresponding to small cratering events or collisions of small bodies (Melosh and Ivanov 2002). Within this time period pressures are beyond the stability range of most of the rock-forming minerals in those meteorites: forsterite, enstatite, feldspars. However, the kinetic barriers are high for transforming these minerals into the polymorphs or decomposition products that represent thermodynamic stability at those pressures. Thus, along the principal Hugoniot of these rocks most of these minerals only develop characteristic deformation features and high densities of defects (Stöffler et al. 2018, for the specific terminology of shock compression: See for instance

Ahrens 1987). Feldspars transform into a dense glass, 'maskelynite', whose structure and density deviate from feldspathic glass synthesized at ambient pressure even after full relaxation of the dynamic stress state. This shock-induced amorphization of feldspars occurs above 30 GPa depending on composition and shock duration (Stöffler et al. 2018). Maskelynite is therefore a 'diaplectic glass' because it has not formed through quenching of a shock-induced melt but through compression of a crystalline material beyond its mechanical stability. It had been suggested that maskelynite in highly shocked meteorites has formed from melt (Chen and El Goresy 2000). However, in many such meteorites the volume fraction of maskelynite is incompatible with conservation of the bulk rock upon release from the shock-compression state if maskelynite had been molten. At very high degrees of dynamic compression the Hugoniot line of the bulk rock intersects the melt line under dynamic compression with subsequent bulk rock melting and disruption of the shocked rock upon release (Ahrens 1986; Stöffler et al. 2018). S7 level meteorites exhibit pervasive melt veins and may reflect sources close to the regions of complete melting (Fritz et al. 2017; Stöffler et al. 2018). Variations in shock levels within given meteorite classes may also reflect different distances to the impact location (Fritz et al. 2017).

Whereas the bulk rock of shocked meteorites only exhibits shock-induced defects and deformation features, locally temperatures are high enough to overcome the kinetic barriers of formation of stable and metastable hP-I and -II minerals. These s.c. hot spots form from collapse of pore spaces and cracks, or represent shock-induced melts that penetrate into fracture zones of the shocked bed rock with velocities that scale with the particle velocity of the shock compression state, or they form through frictional heating along shear zones within the dynamically deforming rock, similar to pseudotachylites along fault surfaces during earthquakes.

In laboratory-scale shock experiments high-pressure mineral formation has only been obtained through collapse of void space (Tschauner et al. 2009) whereas shock-induced friction experiments have not generated any high-pressure minerals (Kenkmann et al. 2000). However, the failure of the latter type of experiments may be owed to the comparatively short duration of ≤ 1 ms of the dynamic compression state in laboratory scale experiments.

In nature we find high-P I and high-P II minerals at the rims or within transformed clasts of shock melt-veins and-pockets in meteorites (see Fig. 8.2 and Table 8.1). Generally, phase occurrence follows the temperature gradient. For instance, in the martian meteorite Tissint a sequence deformed forsterite (Fo80Fay20) → nano-rwd in deformed Fo → ahrensite (out of faylitic rims of the Fo grains) → bridgmanite + wuestite → quenched melt is observed (Ma et al. 2016). (Fig. 8.2 and 8.3a; Table 8.1). In highly shocked chondrites, the highest pressure minerals observed, bridgmanite and akimotoite (Table 8.1), are found in small (≤ 50 μmø) clasts replacing enstatite, whereas larger clasts of enstatite are transformed into majorite (Table 8.1) or contain untransformed enstatite in their kernel. Similarly olivine at the border of the melt vein and in clasts within the vein is transformed to ringwoodite and wadsleyite (two references for many: Tomioka and Miyahara 2017, Hu and Sharp 2017). The melt vein matrix is composed of a jadeitic (Tomioka and Miyahara 2017; Hu and Sharp 2017; Ghosh et al. 2021) or albitic clinopyroxene (Ma et al. 2022d. (Table 8.1),

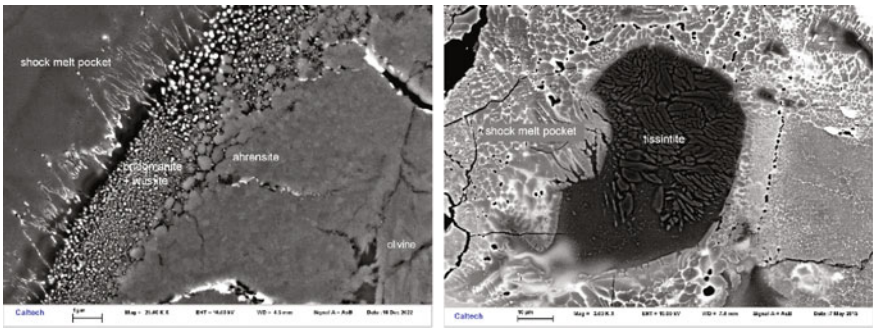

Fig. 8.3 High-pressure minerals ahrensite, bridgmanite, wüstite and tissintite in shock melt pockets from the Tissint Martian meteorite (Ma et al. 2015, 2016)

periclase (Per80-90Wst 10–20), iron, and troillite, and reflects crystallization upon cooling during rarefaction (Tschauner et al. 2014, see Fig. 8.2). In Acfer 040 the shock melt vein matrix contains the high-pressure mineral akimotoite (Sharp et al. 1997, Table 8.1). The release of the dynamic compression state in the shock melt veins is controlled (a) by the release of the shock state in the meteorite parent body (spall or disruption occurs late in the release process, when the stress state drops below the Hugoniot plastic limit of the bedrock) and (b) by temperature release that is controlled by the temperature gradient between the melt and the much cooler bedrock: During dynamic compression the pressure, temperature, and latent heat of shocked melts are correlated, a marked T-gradient implies spatial differences in shock impedance which cause turbulent mixing on the time scale of the particle velocity of the shock compression state (order of few to several km/s) and this turbulent mixing controls the cooling process at high particle velocity (Fig. 8.2). The observation of bridgmanite as mineral in shock-transformed clasts in such veins defines a fiducial point of pressure and temperature and it also constrains the cooling path (Tschauner et al. 2014; Ma et al. 2016) because bridgmanite vitrifies at low pressure at very modest temperatures on fast time scales (Nishi et al. 2022). In sum, the shock release path is divided in three regimes (Fig. 8.2): (a) An initial isentropic release path, (b) a regime of rapid cooling at high pressure controlled by turbulent mixing and T-homogenization of the melt, (c) a modest to low pressure regime at temperatures below 1000 K to nearly ambient. In chondrites the bulk rock Hugoniot pressure appears generally higher than the pressures indicated by the shock melt vein minerals and it has been proposed that the latter form during rarefaction (Fritz et al. 2017; Hu and Sharp 2017). However, it should be noted that the dynamic pressure in a solid and in coexisting melt is generally not equal because part of the shock-induced change in energy is dissipated through the motion and mixing of the melt. Stress equilibration depends on shock-duration and may not be achieved on the time scale of the chondrite-shock metamorpism. In terrestrial impactites this appears to be different (see next section).

In the Martian meteorite class of the shergottites shock-induced melt pockets are much more common than melt veins, indicating either a much shorter duration of the shock-state or formation within the isobaric core of impacts of much smaller scale than the L-chondrite parent body disruption. Models of the probability of escape of ejecta from the gravitation of Mars indicate that the shergottites formed at the outer region of the impact (Head et al. 2002) and indirectly support the former hypothesis. The high-pressure minerals tissintite (hpI), donwilhelmsite (hpII) and stishovite (hpII) (Table 8.1) have been reported from lunar meteorites which are all highly shocked.

8.1.1.2 Terrestrial Impactites

The thick atmosphere of Earth decelerates asteroids that are captured by Earth's gravitation. Only objects of more than 60–100 tons, but depending on impact angle, initial velocity relative to Earth, and density, retain sufficient velocity to generate shock compression in the ground and subsequent crater formation. Many asteroids burst in the higher atmosphere. Hence, the number of terrestrial impacts is comparatively much less than that observed on the Moon or on Mars, even when taking into account that on Earth many craters have been eliminated through later tectonic processes.

Shock states in terrestrial impact craters are assessed through a shock-metamorphic scale that is primarily based on planar deformation features in quartz and feldspars, the transformation of quartz to diaplectic glass (see Stöffler et al. 2018), formation of maskelynite (see above) and high-pressure minerals (Table 8.1). In addition a scale between crater and impactor size allows for estimating dynamic compression states through hydrodynamic modeling. Shock duration in impacts on the scale of the Nördlinger Ries (ø24km), Manicouagan (ø85km), and the Chixculub impact (ø170km) is on the scale of minutes.

High pressure minerals have been found in shocked bedrock (Agarwal et al. 2016) or in xenoliths of bedrock that was trapped in impact breccias (Stähle et al. 2011, 2022) and exhibit a similar fabric as shock meteorites: heavily deformed bed rock, eventually with diaplectic silica and feldspar, and shock melt veins which contain high-pressure minerals and intermediate pressure minerals at their rims. Thus, the overall appearance of shock-metamorphic features in terrestrial impactites is similar to that of highly shocked meteorites. Differences are the result of (a) the different composition of terrestrial continental crust, compared to Martian and lunar crust and to primitive meteorites, and (b) the much longer duration of the dynamic compression state in many terrestrial impactites. In consequence of the longer shock duration the melt vein matrix can contain high-pressure minerals like majoritic garnet (Stähle et al 2011; Ma et al. 2022b) or stöffleritez and albitic clinopyroxene (Ma et al. 2022c). Because of the composition and mineralogy of terrestrial continental crust, partially different, alkaline- and alkline-earth rich high-pressure minerals like zagamiite and accessory high-pressure minerals like high-pressure polymorphs of ilmenite, rutile and zircon are observed in terrestrial impactites but have not been found in meteorites

(El Goresy et al. 2010; Stähle et al. 2011; Tschauner et al. 2020a,b, see Table 8.1). Recently, water-bearing intermediate pressure minerals were reported from shock metamorphized berdrock xenoliths from the Ries (Stähle et al. 2022). Tektites are quenched melted impact ejecta (Stöffler et al. 2018). Their composition is quite similar and more controlled by ion vapor pressure than the bedrock composition (Magna et al. 2011), thus, they are carriers of high-temperature rather than high-pressure minerals. Similarly, and despite their extremely high peak shock pressures, impact melt rocks from the former isobaric core of the impact site and pyroclastic impact melt breccia ('suevite') show generally the imprint of their formation at high temperatures which upon release of the shock state remains high for longer time than the stress state. Thus, these impact-related rocks contain mostly high-temperature minerals although diamond has been found in suevite (El Goresy et al. 2001a, b) and xenoliths of shocked bedrock that are entrapped in suevite contain high-pressure minerals (see above, Table 8.1). Neither in terrestrial nor meteoritic shock-metamorphic mineralogy many minerals without stability field are observed: Lingunite, stöfflerite, and poirierite are the three undisputed cases (Table 8.1). This observation contrasts with the large number of more or less metastable structures that have been computed. The discrepancy is not entirely result of kinetics because of both, terrestrial and meteoritic shock-events lack these occurrences, whereas sub-ms shock experiments have yielded transitory metastable phases of silica (Luo et al. 2001). Rather, the absence of a larger number of transitory silicate phases indicates sterical hindrance of the Si[4] → [6] transformation.

8.1.1.3 High-Pressure Minerals from the Earth's deep mantle

Terrestrial high-pressure minerals from below 410 km depth are essential constituents of Earth but beyond our access. Only diamond and a few inclusions in diamond have been identified as pristine minerals from the deep Earth. Besides diamond the following high-pressure and intermediate-pressure minerals have been identified, that is: both their structure and composition have been described (see Table 8.1): breyite, davemaoite, deltanitrogen, ice-VII, ringwoodite, the 10 Å-phase, further garnets with high majorite component have been reported. In addition, minerals with stability fields that range from ambient to elevated or high pressure such as iron, periclase, jeffbenite, and larnite have been found (e.g. in Stachel et al. 2000). Deltanitrogen is a product of exsolution of N from diamond (Navon et al. 2017). It is remarkable that the remaining four minerals are hydrous (ice-VII) (Tschauner et al. 2018a), ring-woodite., (Gu et al. 2022), and the 10 Å-phase (Huang et al. 2020) or have been found in diamond which contain ice-VII (davemaoite, Tschauner et al. (2021b)). Garnet coexisting with the 10 Å-phase indicates a formation pressure of 14–15 GPa (Huang et al. 2020) based on the independent barometric scales by Collerson et al. (2010) and Tao and Fei (2021). Trace elements of this inclusion gave similar patterns as expected for HiMU-source region (and it is noted that Pb isotopes could not be measured along with trace elements). Because of the high yield strength of diamond, inclusions may retain elevated pressures and high-pressure crystal structures. The remnant pressure

of inclusions at 300 K is the end point of a P–T path whose initial point represents the conditions of entrapment of the inclusion in the growing diamond. Reconstruction of these paths based on isochores (Schrauder and Navon 1993), isomekes (path of stress equilibrium between host and guest phase, e.g. in Anzolini et al. 2016), and paths that account for viscoelastic deformation of the hosting diamond (Wang et al. 2021) have been proposed. Chap. 7 of this book describes diamonds and their inclusions in more detail. The present discussion is constrained to intermediate-and high-pressure minerals (hPI and hPII minerals) that actually have been reported as inclusions in diamonds. Hypothetical retrograde transformation products are not discussed here. The few observations of high-pressure minerals suggest that the Earth's water- and carbon cycle extends into the lower mantle. This point follows from the observation of hydrous minerals, ice-VII (Tschauner et al. 2018a), and ringwoodite (Gu et al. 2022), the fact that these minerals were entrapped in growing diamond, and the tentative assessment of the depth of entrapment. Furthermore, three global horizons of extensive metasomatism may exist in the Earth's mantle are potential hosts of a rich intermediate and high-pressure mineralogy that witnesses mobilization of less common elements and are probed by diamonds. These metasomatic horizons may provide incompatible elements to the upper mantle through active and passive upwellings and are replenished through subduction. The mineralogy of the deep Earth has been thought as void of the rich variety of mineral species that occur at the Earth's surface. Variety of species represents enrichment of less common elements. The three zones of potentially rich mineralogy in the mantle are marked by presence of fluids and melts that allow for mobility of these elements, which then may be enriched in accessory phases: (a) The lithosphere-asthenospheric boundary, (b) possibly the UM-TZ boundary, (c) the TZ-LM boundary and the shallow lower mantle. The mineralogy of the metasomatized lithosphere and the lithosphere-asthenospheric boundary is not discussed in this chapter that is dedicated to high-pressure minerals. It shall only be mentioned that minerals like the silicates Ti-and hydroxyl-clinohumite,the titanates carmichealite, priderite, and minerals of the mathiasite-haggeryite series mark a regime of high fluid mobility and enrichment of incompatible elements in the upper mantle (Haggerty 1991; Wang et al. 1999) and are related to the formation of K-rich volcanism that, in part, carries diamonds to the surface. Diamonds which form in the lithospheric mantle contain ocassionaly minerals whose constituent species are minor or trace elements in the average mante such as goldschmidtite (Meyer et al. 2019) and perovskite. A second global layer of fluid or melt or o horizon that contains regions of fluid and melt enriched in elements that are incompatible in the upper mantle has been proposed to exist at the boundary between the transition zone and the upper mantle (Bercovici and Karato 2003). This hypothesis is consistent the observation of diamond inclusions from that depth that give trace element patterns consistent with at least some types of OIB volcanites (Huang et al. 2020). The partially very alkaline-rich inclusions reported by Stachel et al. (2000) from localities in Southamerica have been hypothesized to originate in the lower mantle (Stachel et al. 2000) but experiments (Litasov et al. 2014; Bulatov et al. 2019; Fedoraeva et al. 2019), geobarometry (Anzolini et al. 2016), and the mineralogy of these inclusions

(Brenker et al. 2021) indicate formation in the deep upper mantle or shallow transition zone, and rather support the hypothesis of an enriched, mobile boundary layer between transition zone and upper mantle than processes in the lower mantle. The observation of ice-VII inclusions (Tschauner et al. 2018a), hydrous ringwoodite (Gu et al. 2022), and K-rich davemaoite (Tschauner et al. 2021b, 2022d) from the deep transition zone or lower mantle suggest a third region of extensive regional mantle metasomatism between 600-860 km depth–given that the assessment of entrapment conditions is correct (Wang et al. 2021; Tschauner et al. 2021b; Gu et al. 2022). However, it is not known if these occurrences represent local, regional or global phenomena in the deep mantle.

8.2 High Temperature Minerals–Definition

The concept of induced changes in valence electron configuration works well for defining high-pressure minerals. Hence, it may be applied to high-temperature minerals as well. The regime of temperatures that induce changes in valence electron configuration is achieved for the solid state at pressures where the melting curves are sufficiently high. However, this regime is barely explored by observation in nature or by experiment. Ringwoodite-Q and ahrensite-Q are silicate spinels with partial inversion and involve a spinel endmember component $Si[]SiO_4$ that makes up to 30 mol% in these minerals. They form as solidus phases in shock-melt pockets of picritic to komatiitic bulk composition (Table 8.1) and may be labeled a intermediate-pressure/temperature phases. In nearly all environments minerals form in paragenesis with other minerals or phases of different composition. Under conditions of very high temperature, redox reactions with gases or coexisting minerals and melts can stabilize redox states that do not occur at temperatures in the common range of igneous or metamorphic processes in the Earth's crust. The temperature-induced intersections of redox reactions at the given O_2-fugacity (Essene and Fisher 1986) provide a criterion for high-temperature minerals that is conceptionally related to the criterion for high-pressure minerals (Sect. 8.1) and describes well the occurrences of minerals in early solar condensates, tektites, fulgurites, and impact melts. It is noted that many of these minerals, carbides, silicides, alloys like cohenite and khamrabaevite (Table 8.2), are not bound to high temperatures-they occur under sufficiently reducing conditions at much lower temperatures or at high pressures as well. Some genuine high-temperature minerals like cristobalite owe their formation to large entropic components. However, the decrease of the vibrational relative to ground state energy with decreasing temperature commonly induces distortive phase transitions or order–disorder transitions such as for cristobalite, tridymite, isocubanite which convert to lower symmetric, partially ordered phases, which are observed as minerals. Many minerals that occur in former high-T environments are likely products of such transitions such as panguite and kangite (Fig. 8.4; Table 8.2). As in the case of high pressures, there are also minerals that have natural stability fields at both, low and high temperatures such as corundum, zircon, baddeleyite, thorite, thortveitite.

In advance of a more rigorous classification we focus here on minerals that form at very high temperature where the relevant redox buffer reactions have stabilized valences that are not stable under typical conditions of igneous and metamorpic processes on Earth. This regime of mineral formation includes presolar minerals, minerals that formed by sublimation in the solar nebula as first or early condensates, minerals in fulgurites, tektites, and former impact melts. The use of modern micro-analysis techniques has greatly extended our knowledge about these minerals which are recognized as carriers of information about processes in the early solar nebula through their isotopic record, trace elements and formation conditions (Rubin and Ma 2017). Presolar minerals can be carriers of isotope anomalies that are result of nucleonic processes during novae or supernovae. Other high temperature minerals occur

Table 8.2 Recently-identified primary high-temperature minerals in refractory inclusions from the solar nebula that have formed by sublimation ('condensates')

Name	Composition	Structure type	Reference
Elements and alloys			
Hexamolybdenum	(Mo,Ru,Fe)	hcp	Ma et al. (2014)
Carbide and nitride			
Khmrabaevite	TiC	Halite	Ma and Rossman (2009a)
Osbornite	TiN	Halite	Ma and Beckett (2020)
Oxides			
Addibischoffite	$Ca_2Al_6Al_6O_{20}$	Rhönite	Ma et al. (2017a)
Allendeite	$Sc_4Zr_3O_{12}$	Allendeite	Ma et al. (2014)
Beckettite	$Ca_2V_6Al_6O_{20}$	Rhönite	Ma et al. (2021b)
Calzirtite	$Ca_2Zr_5Ti_2O_{16}$	Calzirtite	Ma (2020), Xiong et al. (2020)
Kaitianite	$Ti^{3+}{}_2Ti^{4+}O_5$	Oxyvanite	Ma and Beckett (2021)
Kangite	$(Sc,Ti,Al,Zr,Mg,Ca,\square)_2O_3$	Bixbyite	Ma et al. (2013b)
Krotite	$CaAl_2O_4$	$NaBePO_4$	Ma et al. (2011b)
Lakargiite	$CaZrO_3$	Perovskite	Ma (2011)

(continued)

Table 8.2 (continued)

Name	Composition	Structure type	Reference
Louisfuchsite	$Ca_2(Mg_4Ti_2)(Al_4Si_2)O_{20}$	Rhönite	Ma and Krot (2022)
Machiite	$Al_2Ti_3O_9$	Schreyerite	Krot et al. (2020)
Panguite	$(Ti,Al_2,Sc,Mg,Zr,Ca)_{1.8}O_3$	Related to bixbyite-type	Ma et al. (2012)
Sassite	$(Ti^{4+},Ti^{3+},Mg,Sc,Al)_3O_5$	Pseudobrookite	Zhang et al. (2015)
Tazheranite	$(Zr,Ti,Ca,Y)O_{1.75}$	Cubic zirconia	Ma and Rossman (2008)
Tistarite	Ti_2O_3	Corundum	Ma and Rossman (2009a)
Warkite	$Ca_2Sc_6Al_6O_{20}$	Rhönite	Ma et al. (2020)
Silicates			
Baghdadite	$Ca_3(Zr,Ti)Si_2O_9$	Baghdadite	Ma (2018)
Burnettite	$CaV_{3+}AlSiO_6$	Diopside	Ma et al. (2022a)
Davisite	$CaScAlSiO_6$	Diopside	Ma and Rossman (2009b)
Dmisteinbergite	$CaAl_2Si_2O_8$	Dmisteinbergite	Ma et al. (2013a)
Eringaite	$Ca_3Sc_2Si_3O_{12}$	Garnet	Ma (2012)
Grossmanite	$CaTi^{3+}AlsiO_6$	Diopside	Ma and Rossman (2009c)
Kushiroite	$CaAlAlSiO_6$	Diopside	Kimura et al. (2009), Ma et al. (2009)
Mullite	$Al_6Si_2O_{13}$	Mullite	Ma and Rossman (2009a)
Paqueite	$Ca_3TiSi_2(Al,Ti_2Si)_3O_{14}$	$Ca_3(Ga_2Ge)Ge_3O_{14}$	Ma et al. (2022a)
Thortveitite	$Sc_2Si_2O_7$	Thortveitite	Ma et al. (2011a)
Rubinite	$Ca_3Ti_2Si_3O_{12}$	Garnet	Ma et al. (2017c)

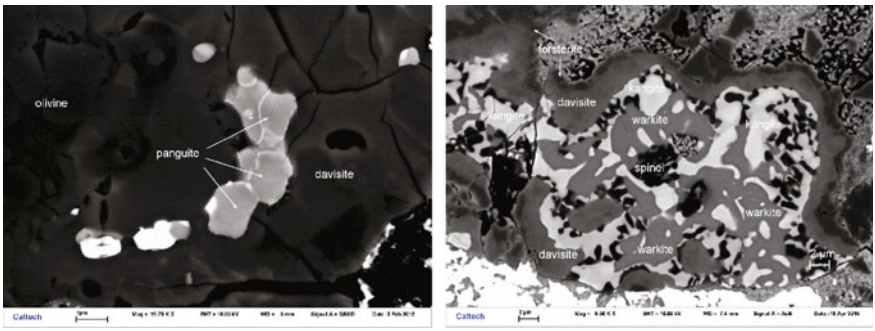

Fig. 8.4 Ultrarefractory minerals panguite and davisite from the Allende CV3 meteorite (Ma et al. 2012), kangite, warkite and davisite from the DOM 08,004 CO3 meteorite (Ma et al. 2020)

in volcanic, i.p. phreatomagmatic, environments and in pyrometamorphic rocks such as the Hatrurim formation in the Near East.

References

Adachi G, Imanaka N (1998) The binary rare earth oxides. Chem Rev 98:1479–1514

Agarwal A, Reznik B, Kontny A, Schilling F (2016) Lingunite – a high-pressure plagioclase polymorph at mineral interfaces in doleritic rock if the Lockne impact structure (Sweden). Sci Rep 6:25991

Ahrens TJ (1986) Application of shock wave data to earth and planetary science. In: Gupta YM (ed) Shock Waves in Condensed Matter. Plenum, New York, pp 571–588

Angel RJ, Chopelas A, Ross NL (1992) Stability of high-density clinoenstatite at upper-mantle pressures. Nature 358:322–324

Anzolini C, Angel RJ, Merlini M, Derzsi M, Tokar K, Milani S, Krebs MY, Brenker FE, Nestola F, Harris JW (2016) Depth of formation of $CaSiO_3$-walstromite included in super-deep diamonds. Lithos 265:138–147. https://doi.org/10.1016/j.lithos.2016.09.025

Armstrong LS, Walter MJ (2012) Tetragonal almandine pyrope phase (TAPP): retrograde Mg-perovskite from subducted oceanic crust? Eur J Min 24:587–597

Armstrong MR et al (2022) Highly ordered graphite (HOPG) to hexagonal diamond (lonsdaleite) phase transition observed on picosecond time scales using ultrafast x-ray diffraction. J Appl Phys 132:055901

Asimow PD, Lin C, Bindi L, Ma C, Tschauner O, Hollister LS, Steinhardt PJ (2016) Shock synthesis of quasiecrystals with implications for their origin in asteroid collisions. Proc Nat Acad Sci USA 113:7077–7081

Beck P, Gillet P, Gautron L, Daniel I, El Goresy A (2004) A new nat ural high-pressure (Na, Ca)-hexaluminosilicate [(CaxNa1 x)Al3+xSi3 xO11] in shocked Martian meteorites. Earth Planet Sci Lett 219:1–12

Bercovici D, Karato S (2003) Whole-mantle convection and the transition-zone water filter. Nature 425:39–44

Bindi L et al (2011) Icosahedrite, $Al_{63}Cu_{24}Fe_{13}$, the first natural quasicrystal. Am Min 96:928–931

Bindi L, Chen M, Xie XD (2017) Discovery of the Fe-analogue of akimotoite in the shocked Suizhou L6 chondrite. Sci Rep 7:42674

Bindi L, Xie XD (2018) Shenzhuangite, $NiFeS_2$, the Ni-analogue of chalcopyrite from the suizhou L6 chondrite. Eur J Min 30:165–169

Bindi L, Brenker FE, Nestola F, Koch TE, Prior DJ, Lilly K, Krot AN, Bizzarro M, Xie X (2019) Discovery of asimowite, the Fe-analog of wadsleyite, in shock-melted silicate droplets of the suizhou L6 and the quebrada chimborazo 001 CB3.0 chondrites. Am Min 104:775–778

Bindi L, Shim S-H, Sharp TG, Xie X (2020) Evidence for the charge disproportionation of iron in extraterrestrial bridgmanite. Sci. Adv. 6: EAAY7893.

Bindi L, Sinmyo R, Bykova E, Ovsyannikov SV, McCammon C, Kupenko I, Ismailova L, Dubrovinsky L, Xie X (2021) Discovery of elgoresyite,$(Mg, Fe)_5Si_2O_9$: implications for novel iron-magnesium silicates in rocky planetary interiors. ACS Earth Space Chem.\ 5:2124–2130

Binns RA, Davis RJ, Reed SJB (1969) Ringwoodite, natural $(Mg, Fe)2Si_O4$ spinel in Tenham meteorite. Nature 221:943–945

Brenker FE, Nestola F, Brenker L, Peruzzo L, Harris JW (2021) Origin, properties, and structure of breyite. Am Min 106:38–43

Britvin SN, Rudashevskii NS, Krivovichev SV, Burns PC, Polekhovsky YS (2002) Allabogdanite, (Fe, Ni)2P, a new mineral from the onello meteorite: the occurrence and crystal structure. Am Min 87:1245–1249

Bulatov VK, Girnis AV, Brey GP, Woodland AB, Höfer HE (2019) Ferropericlase crystallization under upper mantle conditions. Contr Min Petr. https://doi.org/10.1007/s00410-019-1582-6.

Cavosie AJ, Erickson TM, Timms NE (2015) Nanoscale records of ancient shock deformation: reidite ($ZrSiO_4$) in sandstone at the ordovician rock Elm impact crater. Geology 43:315–318

Chao ECT, Shoemaker EM, Madsen MM (1960) First natural occurrence of coesite. Science 132:220–222

Chao ECT, Fahey JJ, Littler J, Milton DJ (1962) Stishovite, SiO_2, a very high pressure new mineral from meteor crater. Arizona J Geophys Res 67:419

Chao ECT (1967) Shock effects, in certain rock-forming minerals. Science 156:192–194

Chen M & El Goresy A (2000) The nature of maskelynite in shocked meteorites: not diaplectic glass but a glass quenched from shock-induced dense melt at high pressures. Earth Planet Sci Lett 179:489–502

Chen M, Shu JF, Mao HK, Xie XD, Hemley RJ (2003) Natural occurrence and synthesis of two new postspinel polymorphs of chromite. Proc Nat Acad Sci USA 100:14651–14654

Chen M, Shu J, Xie X, Tan D (2019) Maohokite, a post-spinel polymorph of $MgFe_2O_4$ in shocked gneiss from the Xiuyan crater in China. Met Planet Sci 54:495–502

Collerson KD, Williams Q, Kamber BS, Omori S, Arai H, Ohtani E (2010) Majoritic garnet: A new approach to pressure estimation of shock events in meteorites and the encapsulation of sub-lithospheric inclusions in diamond. Geochim Cosmochim Acta 74:5939–5957

Daulton TL, Eisenhour DD, Bernatowicz TJ, Lewis RS, Buseck PR (1996) Genesis of presolar diamonds: Comparative high-resolution transmission electron microscopy study of meteoritic and terrestrial nano-diamonds. Geochim Cosmochim Acta 60:4853–4872

Dera P, Prewitt CT, Boctor NZ, Hemley RJ (2002) Characterization of a high-pressure phase of silica from the martian meteorite shergotty. Am Min 87:1018–1023

Dewaele A, et al (2012) High-pressure high-temperature equation of state of KCl and KBr. Phys Rev B 85: 214105. https://doi.org/10.1103/PhysRevB.85.214105

Dobrzhinetskaya LF et al (2009) High-pressure highly reduced nitrides and oxides from chromitite of a Tibetan ophiolite. Proc Nat Acad Sci USA 106:19233–19238

Dobrzhinetskaya LF, Wirth R, Yang JS, Green HW, Hutcheon ID, Weber PK, Grew ES (2014) Qingsongite, natural cubic boron nitride: The first boron mineral from the Earth's mantle. Am Min 99:764–772

Du X, Tse JS (2017) Oxygen packing fraction and the structure of silicon and germanium oxide glasses. J Phys Chem B 121:10726–10732

El Goresy A, Gillet P, Chen M, Künstler F, Graup G, Stähle V (2001) In situ discovery of shock-induced graphite-diamond phase transition in gneisses from the ries crater. Germany Am Min 86:611–621

El Goresy A, Chen M, Gillet P, Dubrovinsky L, Graup G, Ahuja R (2001) A natural shock-induced dense polymorph of rutile with alpha-PbO_2 structure in the suevite from the Ries crater in Germany. Earth Planet Sci Lett 192:485–495

El Goresy A et al (2008) Seifertite, a dense orthorhombic polymorph of silica from the Martian meteorites shergotty and zagami. Eur J Min 20:523–528

El Goresy A, Dubrovinsky LS, Gillet P, Graup G, Chen M (2010) Akaogiite: An ultra-dense polymorph of TiO2 with seven-coordinated titanium, in shocked garnet gneisses from the ries crater, germany. Am. Min. 95:892–895

Essene EJ, Fisher DC (1986) Lightning strike fusion–extreme reduction and metal-silicate immiscibility. Science 234:189–193

Fedoraeva AS, Shatskiy A, Litasov KD (2019) The Join $CaCO_3$-CaSiO3 at 6 GPa with implication to Ca-Rich lithologies trapped by kimberlitic diamonds. High Pressure Res 39:547–560. https://doi.org/10.1080/08957959.2019.1660325

Fritz J, Greshake A, Klementova M, Wirth R, Palatinus L, Trønnes RG, Fernandes VA, Böttger U, Ferrière L (2020) Donwilhelmsite, [$CaAl_4Si_2O_{11}$], a new lunar high-pressure Ca-Al-silicate with relevance for subducted terrestrial sediments. Am Min 105:1704–1711. https://doi.org/10.2138/am-2020-7393

Fritz J, Greshake A, Fernandes VA (2017) Revising the shock classification of meteorites. Met Planet Sci 52:1216–1232

Galuskin EV, Kusz J, Galuskina IO, Książek M, Vapnik Y, Zieliński G (2022) Discovery of terrestrial andreyivanovite, FeCrP, and the effect of Cr and V substitution in barringerite-allabogdanite low-pressure transition. Am Min. (in press)

Gibbs GV, Wang D, Hin C, Ross NL, Cox DF, Crawford TD, Spackman MA, Angel RJ (2012) Properties of atoms under pressure: bonded interactions of the atoms in three perovskites. J Chem Phys 137:164313

Gillet P et al (2000) Natural $NaAlSi_3O_8$-hollandite in the shocked Sixiangkou meteorite. Science 287:1633–1636

Glass BP, Liu SB, Leavens PB (2002) Reidite: An impact-produced high-pressure polymorph of zircon found in marine sediments. Am Min 87:562–565

Ghosh S, Tiwari K, Miyahara M, Rohrbach A, Vollmer C, Stagno V, Ohtani E, Ray D (2021) Natural Fe-bearing aluminous bridgmanite in the Katol L6 chondrite. Proc Nat Acad Sci USA 118: 2108736118. https://doi.org/10.1073/pnas.2108736118

Greenwood RC, Schmitz B, Bridges JC, Hutchison R, Franchi IA (2007) Disruption of the L chondrite parent body: New oxygen isotope evidence from Ordovician relict chromite grains. Met Planet Sci 262:204–213

Gu T, Pamato MG, Novella D, Alvaro M, Fournelle J, Brenker FE, ... & Nestola F (2022) Hydrous peridotitic fragments of Earth's mantle 660 km discontinuity sampled by a diamond. Nature Geoscience, 15(11), 950–954

Haggerty SE (1991) Oxide mineralogy of the upper mantle. Rev Min 25:355–416

Harris J, Hutchison MT, Hursthouse M, Light M, Harte B (1997) A new tetragonal silicate mineral occurring as inclusions in lower-mantle diamonds. Nature 387:486–488

Head JN, Melosh HJ, Ivanov BA (2002) Martian meteorite launch: high-speed ejecta from small craters. Science 298:1752–1756

Hu JP, Sharp TG (2017) Back-transformation of high-pressure minerals in shocked chondrites: low-pressure mineral evidence for strong shock. Geochim Cosmochim Acta 215:277–294

Huang S, Tschauner O, Yang S, Humayun M, Liu W, Gilbert Corder SN, Bechtel HA, Tischler J (2020) HIMU geochemical signature originating from the transition zone. Earth Planet Sci Lett 542:116323. https://doi.org/10.1016/j.epsl.2020.116323

Ivanova MA, Petaev MI, MacPherson GJ, Nazarov MA, Taylor LA, Wood JA (2002) The first known occurrence of calcium monoaluminate, in a calcium aluminum-rich inclusion from the CH chondrite northwest africa 470. Met Planet Sci 37:1337–1444

Kagi H, Lu R, Davidson P, Goncharov AF, Mao HK, Hemley RJ (2000) Evidence for ice VI as an inclusion in cuboid diamonds from high P-T near infrared spectroscopy. Min Mag 64:1089–1097

Kenkmann T, Hornemann U, Stöffler D (2000) Experimental generation of shock-induced pseudotachylites along lithological interfaces. Met Planet Sci 35:1275–1290

Kimura M, Mikouchi T, Suzuki A, Miyahara M, Ohtani E, El Goresy A (2009) Kushiroite, CaAlAlSiO6: a new mineral of the pyroxene group from the ALH 85085 CH chondrite, and its genetic significance in refractory inclusions. Am Min 94:1479–1482

Ko B, Greenberg E, Prakapenka VB, Alp EE, Bi WL, Meng Y, Zhang DZ, Shin SH (2022) Calcium dissolution in bridgmanite in the Earth's deep mantle. Nature 611: 88–90. https://doi.org/10.1038/s41586-022-05237-4

Krot AN, Nagashima K, Rossman GR (2020) Machiite, $Al_2Ti_3O_9$, a new oxide mineral from the Murchison carbonaceous chondrite: a new ultra-refractory phase from the solar nebula. Am Min 105:239–243

Lazarz JD, Dera P, Hu Y, Meng Y, Bina CR, Jacobsen SD (2019) High-pressure phase transitions of clinoenstatite. Am Min 104: 897–904. https://doi.org/10.2138/am-2019-6740

Levien L, Prewitt CT, Weidner DJ (1980) Structure and elastic properties of quartz at pressure. Am Min 65:920–930

Li C, Soh KCK, Wu P (2004) Formability of ABO_3 perovskites. J Alloy Comp 372:40–48

Litasov KD, Shatskiy A, Ohtani E (2014) Melting and subsolidus phase relations in peridotite and eclogite systems with reduced COH fluid at 3–16 GPa. Earth Planet Sci Lett 391:87–99

Luo SN, Tschauner O, Asimow PD, Ahrens TJ (2001) A new dense silica polymorph: A possible link between tetrahedrally and octahedrally coordinated silica. Am Min 86:327–332. https://doi.org/10.2138/am-2004-2-327

Ma C, Rossman GR (2008) Discovery of tazheranite (cubic zirconia) in the allende meteorite. Geochim Cosmochim Acta 72(12S):A577

Ma C, Rossman GR (2009) Tistarite, Ti_2O_3, a new refractory mineral from the allende meteorite. Am Min 94:841–844

Ma C, Rossman GR (2009) Davisite, $CaScAlSiO_6$, a new pyroxene from the allende meteorite. Am Min 94:845–848

Ma C, Rossman GR (2009) Grossmanite, $CaTi^{3+}AlSiO_6$, a new pyroxene from the Allende meteorite. Am Min 94:1491–1494

Ma C, Simon SB, Rossman GR, Grossman L (2009) Calcium Tschermak's pyroxene, $CaAlAlSiO_6$, from the Allende and murray meteorites: EBSD and micro-raman characterizations. Am Min 94:1483–1486

Ma C (2011) Discovery of meteoritic lakargiite ($CaZrO_3$), a new ultra-refractory mineral from the Acfer 094 carbonaceous chondrite. Met Planet Sci 46(S1):A144

Ma C, Beckett JR, Tschauner O, Rossman GR (2011) Thortveitite ($Sc_2Si_2O_7$), the first solar silicate? Met Planet Sci 46(S1):A144

Ma C, Kampf AR, Connolly HC Jr, Beckett JR, Rossman GR, Sweeney Smith SA, Schrader DL (2011) Krotite, $CaAl_2O_4$, a new refractory mineral from the NWA 1934 meteorite. Am Min 96:709–715

Ma C (2012) Discovery of meteoritic eringaite, Ca3(Sc, Y, Ti)2Si3O12, the first solar garnet? Met Planet Sci 47(S1):A256

Ma C, Tschauner O, Beckett JR, Rossman GR, Liu W (2012) Panguite, (Ti4+, Sc, Al, Mg, Zr, Ca)1.8O3, a new ultra-refractory titania mineral from the allende meteorite: synchrotron micro-diffraction and EBSD. Am Min 97:1219–1225

Ma C, Krot AN, Bizzarro M (2013) Discovery of dmisteinbergite (hexagonal $CaAl_2Si_2O_8$) in the allende meteorite: a new member of refractory silicates formed in the solar nebula. Am Min 98:1368–1371

Ma C, Tschauner O, Beckett JR, Rossman GR, Liu W (2013) Kangite, (Sc, Ti, Al, Zr, Mg, Ca,□)2O3, a new ultrarefractory scandia mineral from the allende meteorite: synchrotron micro-laue diffraction and electron backscatter diffraction. Am Min 98:870–878

Ma C, Beckett JR, Rossman GR (2014) Allendeite ($Sc_4Zr_3O_{12}$) and hexamolybdenum (Mo, Ru, Fe), two new minerals from an ultrarefractory inclusion from the allende meteorite. Am Min 99:654–666

Ma C, Tschauner O, Beckett JR, Liu Y, Rossman GR, Zhuravlev K, Prakapenka VB, Dera P, Taylor LA (2015) Tissintite, (Ca, Na,□)$AlSi_2O_6$, a highly-defective, shock-induced, high-pressure clinopy-roxene in the Tissint martian meteorite. Earth Planet Sci Lett 422:194–205

Ma C, Tschauner O, Beckett JR, Liu Y, Rossman GR, Sinogeikin SV, Smith JS, Taylor LA (2016) Ahrensite, gamma-Fe_2SiO_4, a new shock-metamorphic mineral from the tissint meteorite: implications for the tissint shock event on Mars. Geochim Cosmochim Acta 184:240–256

Ma C, Tschauner O (2016) Discovery of tetragonal almandine, (Fe, Mg, Ca, Na)3(Al, Si, Mg)2Si3O12, a new high-pressure mineral in shergotty. Met Planet Sci 51:A434

Ma C, Krot AN, Nagashima K (2017) Addibischoffite, $Ca_2Al_6Al_6O_{20}$, a new calcium aluminate mineral from the Acfer 214 CH carbonaceous chondrite: a new refractory phase from the solar nebula. Am Min 102:1556–1560

Ma C, Tschauner O, Beckett JR (2017b) A new high-pressure calcium aluminosilicate ($CaAl_2Si_{3.5}O_{11}$) in martian meteorites: Another after-life for plagioclase and connections to the CAS phase. 48th Lun Planet Sci Conf 48: 1128.

Ma C, Yoshizaki T, Krot AN, Beckett JR, Nakamura T, Nagashima K, Muto J, Ivanova MA (2017) Discovery of rubinite, $Ca_3Ti^{3+}{}_2Si_3O_{12}$, a new garnet mineral in refractory inclusions from carbonaceous chondrites. Met Planet Sci 52(S1):A6023

Ma C (2018) Discovery of meteoritic baghdadite, $Ca_3(Zr, Ti)Si_2O_9$, in Allende: The first solar silicate with structurally essential zirconium? Met Planet Sci 53(S1):A6358

Ma C, Tschauner O, Beckett JR, Rossman GR, Prescher C, Prakapenke VB, Bechtel HA, McDowell A (2018) Liebermannite, $KAlSi_3O_8$, a new shock-metamorphic, high-pressure mineral from the zagami martian meteorite. Met Planet Sci 53:50–61

Ma C, Tschauner O, Beckett JR (2019a) A closer look at martian meteorites: discovery of the new mineral zagamiite, $CaAl_2Si_{3.5}O_{11}$, a shock-metamorphic, high-pressure, calcium aluminosilicate. 9th Inter Conf Mars 9: 6138.

Ma C, Tschauner O, Beckett JR (2019b) Discovery of a new high-pressure silicate phase, (Fe,Mg,Cr,Ti,Ca,□)$_2$(Si,Al)O_4 with a tetragonal spinelloid structure, in a shock melt pocket from the Tissint Martian meteorite. 50th Lun Planet Sci Conf 50: 1460.

Ma C, Tschauner O, Beckett J, Greenberg E, Prakapenka VB (2019) Chenmingite, $FeCr_2O_4$ in the $CaFe_2O_4$-type structure, a shock-induced, high-pressure mineral in the tissint martian meteorite. Am Min 104:1521–1525

Ma C, Tschauner O, Bindi L, Beckett JR, Greenberg E, Prakapenka VB (2019) A vacancy-rich, partially inverted spinelloid silicate, (Mg, Fe, S_i)2(Si,□)O4, as a major matrix phase in shock melt veins of the Tenham and Suizhou L6 chondrites. Met Planet Sci 54:1907–1918

Ma C (2020) Discovery of meteoritic calzirtite in leoville: a new ultrarefractory phase from the solar nebula. Goldschmidt 2020, Abstract No. 1674.

Ma C, Krot AN, Beckett JR, Nagashima K, Tschauner O, Rossman GR, Simon SB, Bischoff A (2020) Warkite, $Ca_2Sc_6Al_6O_{20}$, a new mineral in carbonaceous chondrites and a key-stone phase in ultrarefractory inclusions from the solar nebula. Geochim Cosmochim Acta 277:52–86

Ma C, Beckett JR (2021) Kaitianite, $Ti^{3+}{}_2Ti^{4+}O_5$, a new titanium oxide mineral from allende. Met Planet Sci 56:96–107

Ma C, Beckett JR, Prakapenka V (2021a) Discovery of new high-pressure mineral tschaunerite, (Fe^{2+})($Fe^{2+}Ti^{4+}$)O_4, a shock-induced, post-spinel phase in the Martian meteorite Shergotty. 52nd Lun Planet Sci Conf 52: 1720.

Ma C, Krot AN, Paque JM, Tschauner O, Nagashima K (2021) Beckettite, $Ca_2V_6Al_6O_{20}$, a new mineral in a type a refractory inclusion from allende and clues to processes in the early solar system. Geochim Cosmochim Acta 56:2265–2272

Ma C, Tschauner O, Beckett JR, Prakapenka V (2021c) Discovery of feiite ($Fe^{2+}{}_2(Fe^{2+}Ti^{4+})O_5$) and liuite ($GdFeO_3$-Type $FeTiO_3$), two new shock-induced, high-pressure minerals in the Martian meteorite Shergotty. 52nd Lun Planet Sci Conf 52: 1681.

Ma C, Krot AN (2022) Louisfuchsite, IMA 2022–024, in: CNMNC Newsletter 68, Eur J Mineral 34. https://doi.org/10.5194/ejm-34-385-2022.

Ma C, Rubin AE (2022) Zolenskyite, $FeCr_2S_4$, a new sulfide mineral from the Indarch meteorite. Am Min 107:1030–1033

Ma C, Beckett JR, Tissot FLH, Rossman GR (2022) New minerals in type a inclusions from allende and clues to processes in the early solar system: paqueite, $Ca_3TiSi_2(Al, Ti, S_i)_{3O}14$, and burnettite, $CaVAlS_iO6$. Met Planet Sci 57:1300–1324

Ma C, Tschauner O, Kong M, Beckett JR, Greenberg E, Prakapenka VB, Lee Y (2022) A high-pressure, clinopyroxene-structured polymorph of albite in highly shocked terrestrial and meteoritic rocks. Am Min 107:625–630

Magna T, Deutsch A, Mezger K, Skala R, Seitz HM, Mizera J, Randa Z, Adolph L (2011) Lithium in tektites and impact glasses: Implications for sources, histories and large impacts. Geochim Cosmochim Acta 75: 2137–2158. https://doi.org/10.1016/j.gca.2011.01.032

Manjon FJ et al (2007) Crystal stability and pressure-induced phase transitions in scheelite AWO(4) (A = Ca, Sr, Ba, Pb, Eu) binary oxides. II: towards a systematic understanding. Phys Stat Sol B 244:295–302

McCormick TC (1986) Crystal-chemical aspects of nonstoichiometric pyroxenes. Am Min 71:1434–1440

Melosh HJ, Ivanov BA (2002) Impact crater collapse. Ann Rev Earth Planet Sci 27: 385–415. https://doi.org/10.1146/annurev.earth.27.1.385

Meyer NA, Wenz MD, Walsh JPS, Jacobsen SD, Locock AJ, Harris JW (2019) Goldschmidtite, (K, REE, Sr)(Nb, Cr) O3: A new perovskite supergroup mineral found in diamond from Koffiefontein, South Africa Am Min 104:1345–1350

Mochalov AG et al (1998) Hexaferrum (Fe, Ru), (Fe, Os), (Fe, Ir)-A new mineral. Zap Vseross Mineral Obshch 127:41–51

Murakami M et al (2004) Post-perovskite phase transition in MgSiO3. Science 304:855–858

Nada R, Catlow CRA, Dovesi R, Pisani C (1990) An ab ignition Hartee-fock study of alpha-quartz and stishovite. Phys Chem Min 17:353–362

Navon O, Wirth R, Schmidt C, Jablon BM, Schreiber A, Emmanuel S (2017) Solid molecular nitrogen (delta-N-2) inclusions in juina diamonds: exsolution at the base of the transition zone. Earth Planet Sci Lett 464:237–247

Nemeth P et al (2014) Lonsdaleite is faulted and twinned cubic diamond and does not exist as a discrete material. Nat Comm 5:5447

Nestola F et al (2016) Tetragonal almandine-pyrope phase, TAPP: finally a name for it, the new mineral jeffbenite. Min Mag 80:1219–1232

Nestola F et al (2018) $CaSiO_3$ perovskite in diamond indicates the recycling of oceanic crust into the lower mantle. Nature 555:237–239

Nishi M et al (2022) Bridgmanite freezing in shocked meteorites due to amorphization-induced stress. Geophys Res Lett 49: 2022GL098231

Oganov AR, Ono S (2004) Theoretical and experimental evidence for a post-perovskite phase of MgSiO3 in Earth's D layer. Nature 430:445–448

Prewitt and Downs, 1998 Prewitt CT, Downs RT (1998) High-pressure crystal chemistry. Rev Min 37:283−317

Price GD et al (1983) Wadsleyite, natural beta-$(Mg, Fe)2Si_O4$ from the peace river Mmeteorite. Can Min 21:29–35

Rahm, M, Ångqvist A, Rahm JM, Erhart P, Cammi R (2020) Non-bonded radii of the atoms under compression. Chem-Phys Chem 21: 2441–2453.

Richet P, Mao HK, Bell PM (1988) Static compression and equation of state of CaO to 1.35 Mbar. J Geophys Res 93: 15279–15288. https://doi.org/10.1029/JB093iB12p15279

Rubin AE, Ma C (2017) Meteoritic minerals and their origins. Chemie der Erde–Geochem 77: 325–385.

Schrauder M, Navon O (1993) Solid carbon-dioxide in a natural diamond. Nature 365:42–44

Shannon RD, Prewitt CT (1969) Coordination and volume changes accompanying high-pressure phase transformations of oxides. Mat Res Bull 4:57–59

Shannon RD (1976) Revised effective ionic-radii and systematic studies of interatomic distances in halides and chalcogenides. Acta Cryst A 32:751–767
Sharp TG, Lingemann CM, Dupas C, Stöffler D (1997) Natural occurrence of $MgSiO_3$-ilmenite and evidence for $MgSiO_3$-perovskite in a shocked L chondrite. Science 280:352–355
Sharp TG, DeCarli PS (2006). Shock effects in meteorites, In: Meteorites and the Early Solar System II. Publisher: University of Arizona Press, Tucson, pp 653-677.
Smith JV, Mason B (1970) Pyroxene-garnet transformation in coorara meteorite. Science 168:832–834
Stachel T et al (2000) Kankan diamonds (Guinea) II: lower mantle inclusion parageneses. Contrib Min Petr 140:16–27
Stähle V, Altherr R, Nasdala L, Ludwig T (2011) Ca-rich majorite derived from high-temperature melt and thermally stressed hornblende in shock veins of crustal rocks from the Ries impact crater (Germany). Contrib Min Petr 161:275–291
Stähle V, Chanmuang NC, Schwarz WH, Trieloff M, Varychev A (2022) Newly detected shock-induced high-pressure phases formed in amphibolite clasts of the suevite breccia (Ries impact crater, Germany): Liebermannite, kokchetavite, and other ultrahigh-pressure phases. Contrib Min Petr 177(8), 80
Stöffler D, Hamann C, Metzler K (2018) Shock metamorphism of planetary silicate rocks and sediments: proposal for an updated classification system. Met Planet Sci 53:5–49
Taggart JE, Foord E, Rosenzweig A, Hanson T (1988) Scrutinyite, natural occurrences of alpha PbO_2 from bingham, new mexico. Can Min 26:905–910
Tao R, Fei YW (2021) Recycled calcium carbonate is an efficient oxidation agent under deep upper mantle conditions. Comm Earth Environ 1. https://doi.org/10.1038/s43247-021-00116-8.
Tomioka N, Fujino K (1997) Natural (Mg, Fe)SiO3-ilmenite and -perovskite in the Tenham meteorite. Science 277:1084–1086
Tomioka N, Fujino K (1999) Akimotoite, (Mg, Fe)SiO(3), a new silicate mineral of the ilmenite group in the Tenham chondrite. Am Min 84:267–271
Tomioka N, Miyahara M (2017) High-pressure minerals in shocked meteorites. Met Planet Sci 52:2017–2039
Tomioka N, Bindi L, Okuchi T, Miyahara M, Iitaka T, Li Z, Kawatsu T, Xie X, Porevjav N, Tani R, Kodama Y (2021) Poirierite, a dense metastable polymorph of magnesium iron silicate in shocked meteorites. Comm Earth & Environ 2:1–8
Tschauner O et al (2009) Ultrafast growth of wadsleyite in shock-produced melts and its implications for early solar system impact processes. Proc Nat Acad Sci USA 106:13691–13695
Tschauner O, Ma C, Beckett JR, Prescher C, Prakapenka VB, Rossman GR (2014) Discovery of bridgmanite, the most abundant mineral in earth, in a shocked meteorite. Science 6213:1100–1102. https://doi.org/10.1126/science.1259369
Tschauner O et al (2018a) Ice-VII inclusions in diamonds–evidence for aqueous fluid in the Earth's deep mantle. Science 359:1136–1139
Tschauner O, Ma C, Prescher C, Prakapenka VB (2018b) Structure analysis and conditions of formation of akimotoite in the Tenham chondrite. Met Planet Sci 53:62–74
Tschauner O (2019) High-pressure minerals. Am Min 104: 1701–1731. https://doi.org/10.2138/am-2019-6594.
Tschauner O, Ma C, Lanzirotti A, Newville MG (2020) Riesite, a new high pressure polymorph of TiO_2 from the ries impact structure. Minerals 10:78
Tschauner O, Ma C, Newville MG, Lanzirotti A (2020) Structure analysis of natural wangdaodeite-$LiNbO_3$-Type $FeTiO_3$. Minerals 10:1072
Tschauner O, Ma C, Spray JG, Greenberg E, Prakapenka VB (2021a). Stöfflerite, (Ca, Na)(Si, Al) $_4O_8$ in the hollandite structure: a new high-pressure polymorph of anorthite from martian meteorite NWA 856. Am Min 106: 650-655
Tschauner O, Huang S, Yang S, Humayun M, Liu W, Gilbert Corder SN, Bechtel HA, Tischler J, Rossman GR (2021) Discovery of davemaoite, $CaSiO_3$-Perovskite, as a mineral from the lower mantle. Science 6569:891–894. https://doi.org/10.1126/science.abl8568

Tschauner O (2022a) An observation related to the pressure dependence of ionic radii. Geosciences 12:246. https://doi.org/10.3390/geosciences12060246

Tschauner O (2022b) Corresponding states for volumes of elemental solids at their pressures of polymorphic transformation crystals 12: 1698. https://doi.org/10.3390/cryst12121698

Tschauner O, Navon O, Schmidt C (2022c) Deltanitrogen, IMA 2019–067b, in: CNMNC Newsletter 69, Eur J Mineral 34: 463. https://doi.org/10.5194/ejm-34-463-2022.

Tschauner O, Huang S, Humayun M, Liu W, Rossman GR (2022d) Response to Comment on 'Discovery of Davemaoite, $CaSiO_3$-Perovskite, as a mineral from the lower mantle'. Science 6593. https://doi.org/10.1126/science.abo2029.

Walter MJ, KohnSC PDG, Shirey SB, Speich L, Stachel T, Thomson AR, Yang J (2022) Comment on 'discovery of davemaoite, $CaSiO_3$-perovskite, as a mineral from the lower mantle.' Science 376(6593):590–590

Wang LP, Essene EJ, Zhang YX (1999) Mineral inclusions in pyrope crystals from garnet ridge, arizona, USA: implications for processes in the upper mantle. Contr Min Petr 135:164–178

Wang W, Tschauner O, Huang S, Wu Z, Meng Y, Bechtel HA, Mao HK (2021) Coupled deep-mantle carbon-water cycle: evidence from lower-mantle diamonds. The Innovation 2:100117. https://doi.org/10.1016/j.xinn.2021.100117

Willgallis A, Siegmann E, Hettiaratchi T (1983) Srilankite, a new Zr-Ti-oxide mineral. N Jahrb Min 4:151–157

Woodland AB, Schollenbruch K, Koch M, Ballaran TB, Angel RJ, Frost DJ (2013) Fe_4O_5 and its solid solutions in several simple systems. Contrib Min Petr 166:1677–1686

Xie XD, Chen M, Wang DQ (2001) Shock-related mineralogical features and P-T history of the Suizhou L6 chondrite. Eur J Min 13:1177–1190

Xie XD, Minitti ME, Chen M, Mao HK, Wang DQ, Shu JF, Fei YW (2003) Tuite, gamma-$Ca_3(PO_4)_2$: a new mineral from the Suizhou L6 chondrite. Eur J Min 15:1001–1005

Xie X, Gu X, Yang H, Chen M, Li K (2020) Wangdaodeite, the $LiNbO_3$ -structured high-pressure polymorph of ilmenite, a new mineral from the Suizhou L6 chondrite. Met Planet Sci 55:184–192

Xiong Y, Zhang A-C, Kawasaki N, Ma C, Sakamoto N, Chen J-N, Gu L-X, Yurimoto H (2020) Mineralogical and oxygen isotopic study of a new ultrarefractory inclusion in the Northwest Africa 3118 CV3 chondrite. Met Planet Sci 55:2164–2205

Zhang AC, Ma C, Sakamoto N, Wang RC, Hsu WB, Yurimoto H (2015) Mineralogical anatomy and implications of a Ti–Sc-rich ultrarefractory inclusion from sayh al uhaymir 290 CH3 chondrite. Geochim Cosmochim Acta 163:27–29

Zhu Q, Oganov AR, Lyakhov AO (2013) Novel stable compounds in the Mg-O system under high pressure. Phys Chem Chem Phys 15:7696–7700